INTERNATIONAL JOURNAL OF HYDROGEN ENERGY 41 (2016) 7676–7690

Available online at www.sciencedirect.com

ScienceDirect

journal homepage: www.elsevier.com/locate/he

Hydrogen permeation characteristic of nanoscale passive films formed on different zirconium alloys

Cheng Zeng [a], *Yunhan Ling* [a,*], *Yakui Bai* [a], *Ruiqian Zhang* [b], *Xun Dai* [b], *Yixiang Chen* [c]

[a] *Lab of Advanced Materials, School of Materials Sciences and Engineering, Tsinghua University, Beijing 100084, China*

[b] *Reactor Fuel and Materials Laboratory, Nuclear Power Institute of China, Chengdu 610041, China*

[c] *Technical Institute of Physics and Chemistry, Chinese Academy of Sciences, Beijing 100190, China*

ARTICLE INFO

Article history:
Received 16 August 2015
Received in revised form
25 December 2015
Accepted 14 January 2016
Available online 24 March 2016

Keywords:
Zircaloy
Passive film
Hydrogen permeation
Electrochemistry

ABSTRACT

Zircaloys, rooted in their inherent passivity, are widely used as the cladding materials for light water reactors (LWRs) due to their desirable corrosion resistance against high temperature and high pressure water. The hydrogen permeation behavior on zircaloy with passive film, however, is rarely understood so far. In this work, the gaseous hydrogen permeation characteristic mainly on the defect evolution of nanoscale passive films of nanoscale passive films formed hydrothermally on different types of zirconium alloys (Zirconium, Zircaloy-4, N18 and M5) was explored and compared. Surface analytical techniques were implemented to evaluate the hydrogen permeation characteristic. The AES depth profiles showed that the as-prepared oxides were hundreds of nanometers in thickness and inward diffusion occurred upon hydrogen exposure. Electrochemical measurements suggested that the oxides formed on different types of zircaloys were of similar phase structures of monoclinic zirconia but with different oxygen vacancy concentrations. XPS results comparison confirmed that niobium enhances the hydrogen resistance of the oxides, yet tin causes degradation of the oxides in the reductive environment. In view of these analyses, the involving mechanism was first proposed and discussed on the basis of point defect reactions.

Introduction

In light water reactors (LWR), the surface reaction of the fuel cladding with water results in the oxidation of the cladding and the subsequent release of hydrogen. Fractional released hydrogen was picked-up and diffused into the matrix, causing the formation of hydrogen precipitates. In fusion reactor blanket, structural materials were also confronted with the similar problem of high permeation of hydrogen isotopes in the operational condition, yielding the so-called hydrogen degradation (HD) of the matrix [1].

It is well-known that HD is one of the most important issues in safety regulation for nuclear power plants since it frequently brings a substantial loss of plasticity and sometimes in a decrease in mechanical strength [2,3]. Intensive

* *Corresponding author*. Tel.: +86 1062772856; fax: +86 1062772507.
E-mail address: yhling@mail.tsinghua.edu.cn (Y. Ling).

http://dx.doi.org/10.1016/j.ijhydene.2016.01.174

investigations, pertaining to the hydrides formation and hydrogen permeation through alloys, have already been reported in literature [4–7]. Thus, reduction of hydrogen permeation is an important issue to optimize the tritium balance and minimize hydrogen embrittlement of container [7,8]. An effective coating termed tritium permeation barriers (TPB) has shown significant suppression of hydrogen isotope permeability. The most commonly utilized coatings are alumina coatings, especially the alpha alumina coatings [9,10]. However, previous study has reported that the transformation to the thermodynamically stable phase of alumina coatings occurs at a high temperature (over 1000 °C), which will result in the so-called sensitization effect of the structural materials [11,12].

In the past few decades, the waterside corrosion of zircaloys has been intensively studied and passive films could be easily formed on zircaloys. Zirconium oxide layers have been reported to be conducible to resisting the hydrogen permeation due to the existence of the O–H bonds and theoretical analysis indicated that a 5 nm layer of oxides can reduce the ingress of hydrogen dramatically [13–15]. In spite of several studies using electrochemical methods made on the hydrogen permeation performance in zirconium oxide scales [16,17], the effect of alloying elements on the hydrogen permeation behavior on zircaloy with passive film, however, is rarely understood so far.

In the present study, the experimental procedure was simplified, as possible, to avoid unnecessary influences. The gaseous hydrogen permeation characteristic of oxides formed hydrothermally on different types of zirconium alloys (Zirconium, Zircaloy-4, N18 and M5) was explored. The surface morphology, phase and chemical composition distribution along the depth were studied and compared for the four different types of zircaloys. Interestingly, we found that the performance of gaseous hydrogen permeation varies with the different alloying elements and based on these phenomena, the involving mechanism was proposed and discussed.

Experimental details

The specimens used in this study are recrystallized zircaloys provided by Nuclear Power Institute of China, including zirconium, zircaloy-4 (Zr-4), N18 and M5. The dimension and chemical composition of the samples are listed in Table 1. It should be mentioned that except for Zr, the other three zircaloys all contain precipitates. Precipitates in Zr-4 are reported to be $Zr(Fe, Cr)_2$, precipitates in N18 are reported to be $Zr(Nb, Fe)_2$ and $Zr(Nb, Fe, Cr)_2$, while the precipitate type of M5 is β-Nb [18].

Samples were mechanically ground with SiC paper of grit sizes ranging from 500 to 5000, and then polished with diamond paste down to 0.5 μm. The microstructure of the as-received alloys was examined by a polarized light optical microscope (OM, 6XB-PC, China). Prior to OM observations, the alloys were etched using a solution of 45 vol.% H_2O + 45 vol.% HNO_3 + 10 vol. HF.

The oxide films were prepared in an autoclave filled with pure water at 200 °C for 24 h under a saturation pressure of ~1.3 MPa. As for hydrogen permeation process, parts of the as-prepared samples was sealed in quartz tubes with hydrogen pressure of 5000 Pa at room temperature and then heated at 300 °C for 4 h. To make it concise, the as-prepared oxides are henceforth denoted as NH and the samples after hydrogen permeation are denoted as YH, e.g. as for Zr, the oxide layers before and after hydrogen permeation are denoted as Zr-NH and Zr-YH, respectively.

Phase identification of the oxide layers was performed with a Raman spectrometer (Lab HR Evolution, HORIBA, France) using argon ion laser excitation at 532.2 nm at room temperature. Surface morphologies of the films were examined by field emission scanning electron microscopy (FE-SEM, JSM-7001F, JEOL, Japan) with energy dispersive spectroscopy (EDS). The main elemental distribution along the cross section was measured by Auger electron spectroscopy (AES, PHI-700, ULVAC-PHI, Japan), equipped with a coaxial electron gun, CMA energy analyzer and a differentially pumped Ar ion gun. The Photoluminescence (PL) characteristic using a 325 nm laser was employed at room temperature with the same Raman spectrometer mentioned above. X-ray photoelectron spectroscopy (XPS, ESCALAB 250Xi, ThermoFisherSCIENTIFIC, US) was used with a monochromatic Al X-ray source of 15 kV, 45 W. The pressure during XPS analysis was less than 1×10^{-6} Pa and all spectra were referenced to C 1s peak of adventitious hydrocarbon at 284.60 eV [19]. The XPS spectra are curve-fitted with a combination of Gaussian and Lorentzian line shapes, using a Shirley-type background substration.

All the Electrochemical results were recorded in a three-electrode cell with a universal electrochemical interface analyzer (IM6E, ZAHNER, Germany). The samples, which are also the working electrode, were embedded in a two-component epoxy resin with the platinum foil acting as the counter electrode and the saturated calomel electrode (SCE) as the reference electrode. All experiments were performed at ambient temperature in 0.1 M Na_2SO_4. The electrochemical impedance spectroscopy (EIS) test was carried out using an excitation voltage of 10 mV (peak-to-peak) and an applied

Table 1 – Dimension and chemical composition of the as-received zircaloys

Specimens	Dimension (mm)	Alloy elements (wt.%)					
		Sn	Nb	Fe	Cr	O	Zr
#1 (Zr)	10 × 10 × 2	–	–	–	–	–	Bal.
#2 (Zr-4)	⌀ 8.2 × 1.6	1.52	–	0.18	0.09	0.10	Bal.
#3 (N18)	10 × 10 × 1	1.04	0.34	0.30	0.10	0.12	Bal.
#4 (M5)	15 × 15 × 0.6	–	0.98	0.03	–	0.13	Bal.

frequency from 1 MHz to 0.01 Hz. The capacitance of the interface was measured at constant frequency of 1 kHz at a sweep rate of 50 mV/s.

Results and discussion

Morphology, phase and depth analysis

The optical morphology of the oxides is shown in Fig. 1. We can see that all the alloys displayed recrystallized equiaxed grains. Compared to zirconium with the average grain size of ~30 μm, the other three alloys displayed much smaller grain sizes of ~4 μm. The surface morphologies of the oxide layers for different zircaloys are depicted in Fig. 2. It was clear that oxides formed on different zircaloys have an almost identical surface morphology before and after hydrogen permeation, with irregular pores and micro-cracks dispersed in the outer oxide layer. The formation of pores and micro-cracks could be ascribed to the release of thermal stress due to the transition of tetragonal to monoclinic ZrO_2 as reported by McIntyre et al. [20] and Cox et al. [21].

Fig. 3 shows the Raman spectra of the oxide layers for different zircaloys. It was found that the Raman spectra of the as-prepared oxides give major bands at around 173, 337, 475 and 634 cm^{-1}. The Raman bands at 173 and 337 cm^{-1} are exclusively assigned to the monoclinic phase of ZrO_2, while the bands at 475 and 634 cm^{-1} are common for both the tetragonal and monoclinic phase [22,23]. The characteristic peaks of t-ZrO_2 at 149, 269 and 312 cm^{-1} were however absent in the spectra. Therefore, the Raman spectra suggest that the as-prepared oxide layers are predominately composed of m-ZrO_2. It is clear the main phase of the oxides remained intact after hydrogen permeation.

The depth profiles of Zr and O in the oxides before and after hydrogen permeation was plotted in Fig. 4. The oxides before and after hydrogen permeation are denoted with solid and dash lines, respectively. The AES results revealed that the thickness of oxides formed on different zircaloys kept almost the same after hydrogen permeation, around 800, 600, 400 and 500 nm for the oxides formed on Zr, Zr-4, N18 and M5, respectively. From the viewpoint of film growth, N18 has the highest corrosion resistance while zirconium has the lowest corrosion resistance. The results reported by Zhou and co-workers who claimed that the formation of precipitates Zr–Fe–Nb rather than Zr–Fe–Cr or β-Nb could significantly enhance the corrosion resistance of zircaloys [24], are in good accordance with the AES results.

From AES profiles, it can be seen that the total amount of oxygen in the oxides increased after hydrogen permeation, and the reason for that was probably due to the absorbed hydroxyl oxygen. Interestingly, an overall inward diffusion of oxygen after hydrogen permeation, as marked by the blue arrows, was exhibited, though subtle differences still existed for the four different types of zircaloys. Taking into account the different chemical compositions of these four zircaloys, it is safe to infer that the alloying element of tin or niobium may be related to the different behavior of oxygen ions during the hydrogen permeation process.

Electrochemical measurements

Electrochemical impedance spectroscopy

It should be noted that all the measurements were carried out after holding the open circuit potential constant for 3 h. EIS measurements were utilized to investigate the response from the structure of the oxides before and after hydrogen permeation. Since the stability of the electrochemical system during EIS measurement is critical to obtaining credible data. The

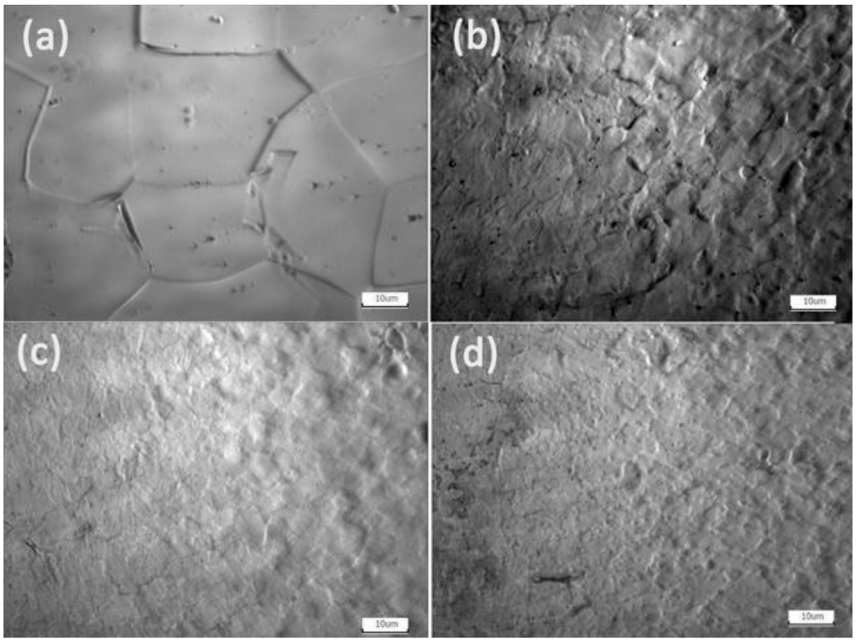

Fig. 1 – The optical microscopy of the as-received zircaloys: (a) Zr, (b) Zr-4, (c) N18, and (d) M5.

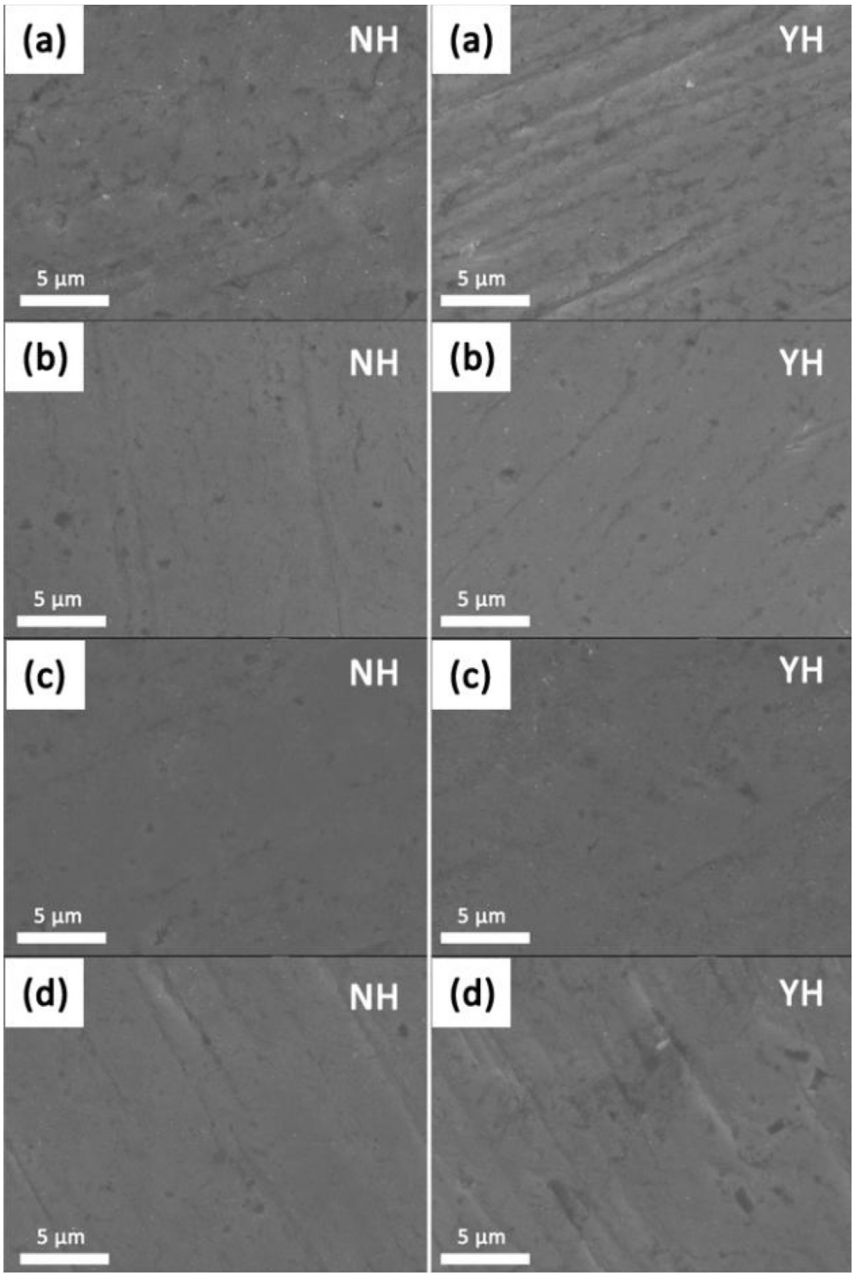

Fig. 2 – The surface morphologies of the oxides formed on different zircaloys before and after hydrogen permeation: (a) Zr, (b) Zr-4, (c) N18, and (d) M5.

data were checked experimentally by sweeping the frequencies from high-to-low and then immediately back from low-to-high to ascertain that the same impedance values were obtained at equivalent frequencies in the two directions. If the test system is in the steady state, the impedance data should match in the two step directions. A coincidence was observed in all impedance measurements.

It is well documented in the literature that at frequencies higher than 1 kHz, the measured capacitance was almost independent of frequency, displaying an almost purely capacitive frequency response [25]. Film thickness of the oxides was calculated from the capacitance measured at frequencies of 1 kHz. Therefore, the well-known 'parallel plate' expression for the capacitance was used to estimate the equivalent thickness L.

$$L = \frac{\varepsilon\varepsilon_0}{C} \quad (1)$$

where ε_0 is the vacuum permittivity (8.85×10^{-14} F/cm) and $\varepsilon = 22$ [26] is the relative dielectric constant of the ZrO_2 passive film (the same value is assumed for the films after hydrogen permeation as the Raman spectra have proved that the predominate phase of the oxide layer remains unchanged). The interfacial capacitance C is obtained from $C = -\frac{1}{\omega Z''}$, where ω is the angular frequency, i.e. $\omega = 2\pi f$ and Z'' is the imaginary part

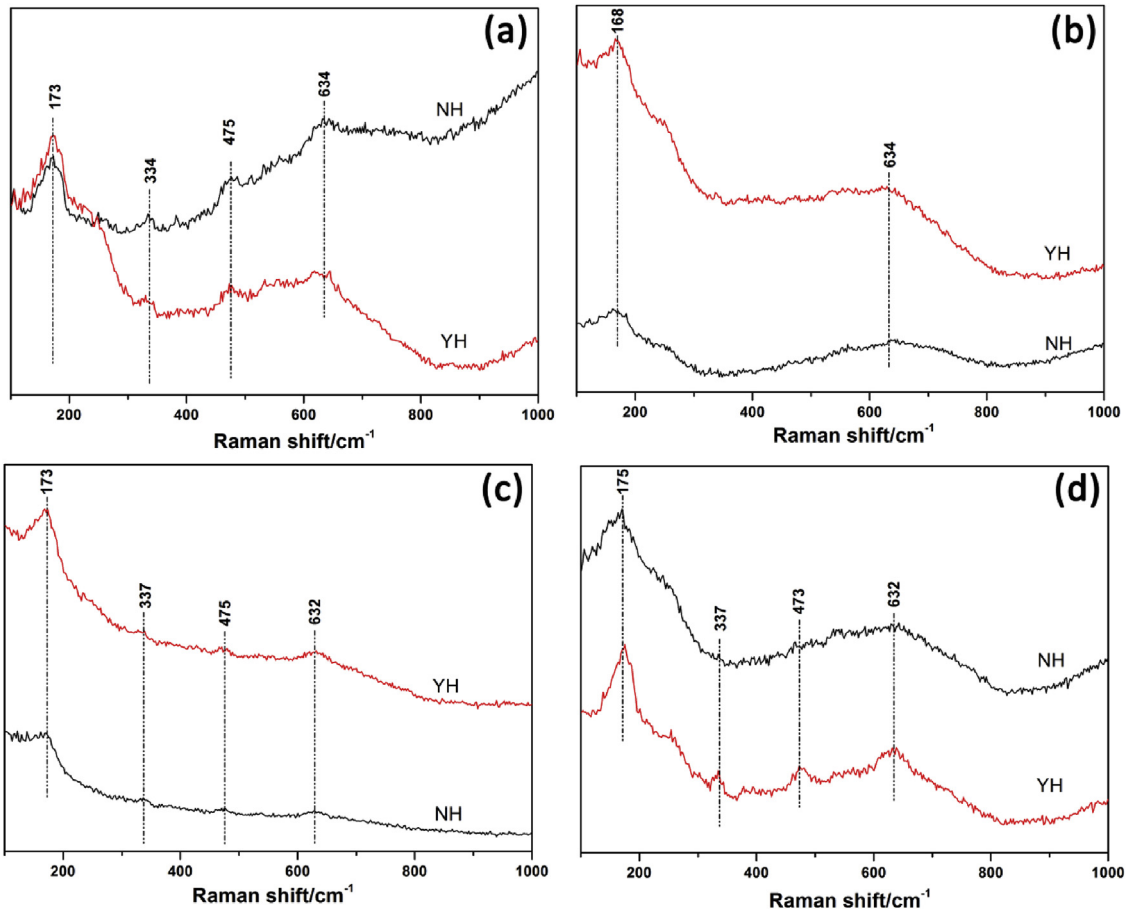

Fig. 3 – Raman spectra of the oxides formed on different zircaloys before and after hydrogen permeation: (a) Zr, (b) Zr-4, (c) N18, and (d) M5.

of the impedance. The equivalent thickness is summarized in Table 2. It is clear that the calculated thickness is similar for the oxides formed on different zircaloys, but, far smaller than the actual thickness determined by the depth profiles. It probably related to the roughness of the surface and the EIS reflected the only 'compact' passive film.

Fig. 5 depicts the Bode plots of the oxide layers for different zircaloys before and after hydrogen permeation. The similar shape of Bode plots suggests that all the as-prepared oxides have a similar oxide structure, i.e. an outer porous layer and an inner dense layer.

From the Bode plots, we can see that the phase angle evolves between 60° and 85° in the lower frequency (<1 KHz), which means that the oxide is mainly capacitive. The magnification of phase plots in lower frequency range shows two slopes, indicating the presence of two capacitive layers (the outer layer is relatively porous and insulated while the inner barrier layer is dense and defective [25,27]), as previously reported for the passive film formed on zirconium in 1 M H_3PO_4 [27]. Given that the estimated thickness is far smaller than the actual thickness, it is assumed that the inner dense layer is much thinner than the outer porous layer. It should be emphasized that the slope at very low frequency generally relates to the slowest process like ion diffusion through the inner dense layer, and inversely the slope at the medial frequency normally corresponds to the faster process, such as the electron transportation and the ion diffusion through the outer porous layer [28].

Compared to the as-prepared oxide layers, it is clear that the magnitude of the impedance was larger after hydrogen permeation except for the oxides of Zr-4, showing an inverse change. From the phase angle variation in the lower frequency range, we can see that the change of 'compacity' after hydrogen permeation for different zircaloys is different. The summarized results of the 'compacity' change are listed in Table 3. From the EIS results, one can see that the M5-NH transformed to a more compact layer after hydrogen permeation, while Zr-4-NH transformed to a less protective one. As for Zr-NH and N18-NH, the outer and inner layer shows an inverse 'compacity' change.

Mott–Schottky analysis

As mentioned above, it is assumed that the impedance is dominated by the outer porous oxide layer while the semiconductor properties mainly depend on the inner barrier layer. Generally, according to Mott–Schottky (MS) theory [29], the space charge capacitances of n-type and p-type semiconductor junctions are given by

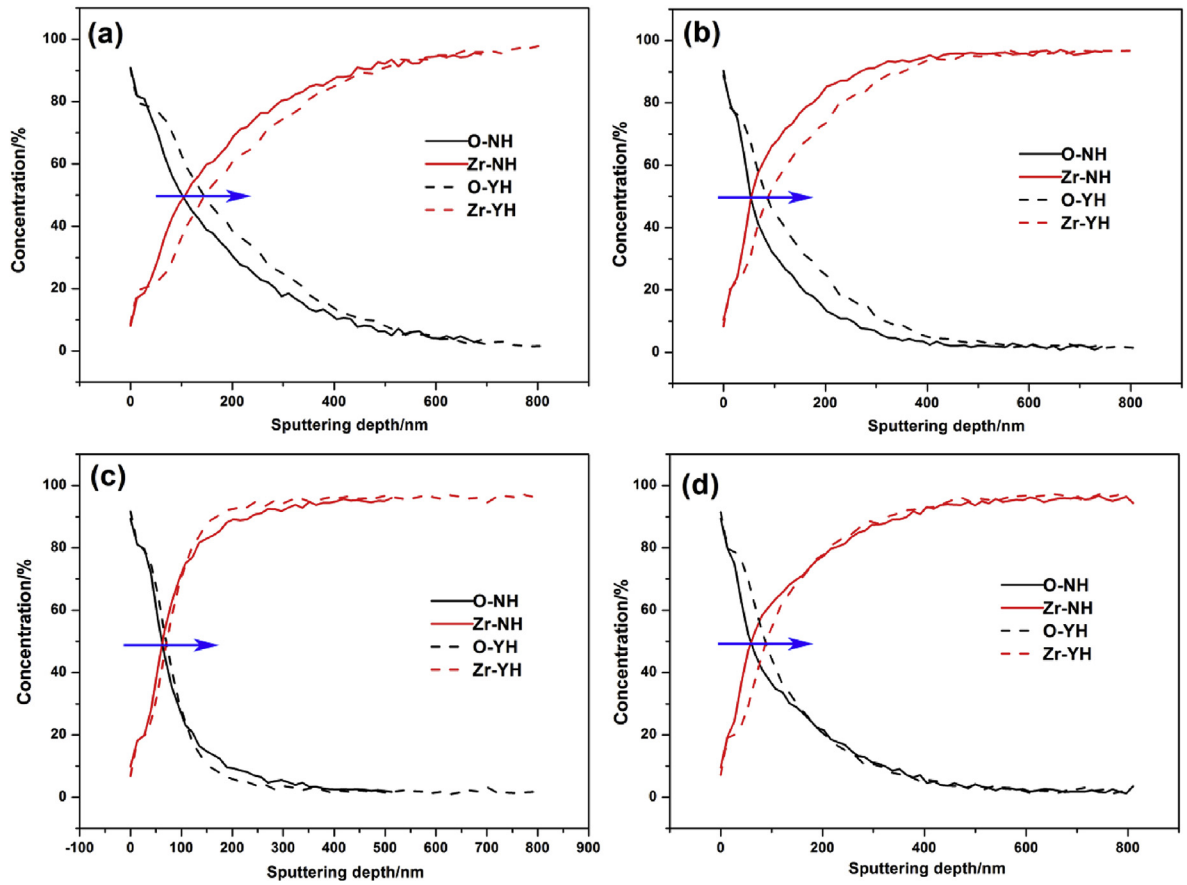

Fig. 4 – The depth profiles of Zr and O for the oxides formed on different zircaloys before and after hydrogen permeation: (a) Zr, (b) Zr-4, (c) N18, and (d) M5.

Table 2 – Estimated thickness for samples before and after hydrogen permeation.

Samples	Estimated thickness (nm)	
	NH	YH
Zr	16.8	23.9
Zr-4	15.4	16.9
N18	15.4	22.9
M5	13.9	18.0

$$\frac{1}{C_{sc}^2} = \frac{2}{\varepsilon\varepsilon_0 q N_D}\left(V - V_{fb} - \frac{kT}{q}\right) \quad n-type \tag{2}$$

and

$$\frac{1}{C_{sc}^2} = \frac{-2}{\varepsilon\varepsilon_0 q N_A}\left(V - V_{fb} - \frac{kT}{q}\right) \quad p-type \tag{3}$$

Respectively, where N_D/N_A is the donor/acceptor concentration (cm^{-3}), ε_0 and ε has been explained in the Eq. (1). V is the applied potential, V_{fb} is the flat band potential, q is the electron charge, and kT/q is about 25 mV at room temperature. Actually, the measured capacitance cannot be directly approximated as the space charge capacitance. Instead, the capacitance of the whole oxide can be regarded as a series combination of a voltage-independent capacitance and the space charge capacitance C_{bl}, as reported by Chen et al. and Dutoit et al. [25,30]. Therefore, the formula should be rewritten as:

$$\frac{1}{C^2} = \frac{1}{C_{OX}^2} + \frac{2}{\varepsilon\varepsilon_0 q N_D}\left(V - V_{fb} - \frac{kT}{q}\right) \quad n-type \tag{4}$$

where the notation is the same as previously defined. Therefore the slope of MS-plot is not influenced by C_{ox} and thus the donor density can still be derived from the slope. Fig. 6 shows the Mott–Schottky plots for the films before and after hydrogen permeation. From the positive slopes, it is concluded that the passive films formed on different zircaloys before or after hydrogen permeation exhibits n-type electronic character, indicating that the dominant defects in the films are oxygen vacancies.

The donor density was calculated from Eq. (2) for different oxide films before and after hydrogen permeation. The results were summarized in Fig. 7. It was found that the donor concentration, N_D, which in the range of 10^{19}–10^{20} cm^{-3}, is almost two-orders higher than that of the results reported by Chen et al. [25] and Meisterjahn et al. [31]. The much higher donor concentration demonstrates that the barrier oxide layer is highly-doped with electron donors, probably due to the ultra-small thickness of the inner defective layer, which is well consistent with the above conclusions. Furthermore, it can be seen that amongst the as-prepared oxide films, Zr-NH has the lowest donor concentration, Zr-4-NH, N18-NH, higher and M5-

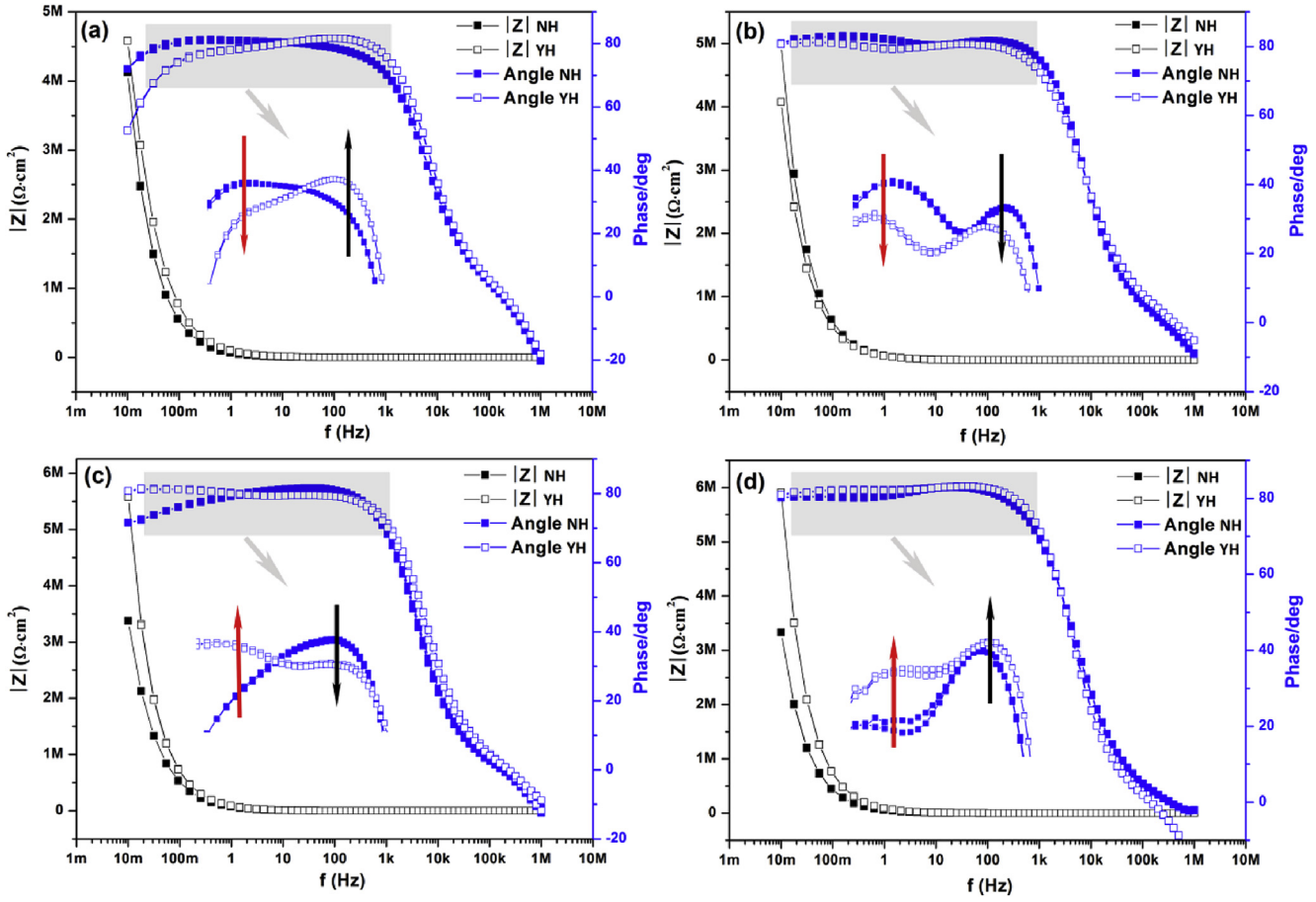

Fig. 5 – Bode plots for the oxides formed on different zircaloys before and after hydrogen permeation: (a) Zr, (b) Zr-4, (c) N18, and (d) M5.

Table 3 – 'Compacity' change of the oxides for different zircaloys after hydrogen permeation.

Samples	'Compacity' change (↑ or ↓)	
	Outer layer	Inner layer
Zr	↑	↓
Zr-4	↓	↓
N18	↓	↑
M5	↑	↑

NH has the highest N_D. After hydrogen permeation, the donor density of Zr-4-YH however is almost three-folds larger than that of Zr-4-NH, while the N_D of NH, the N_D of M5-YH decreased from 2×10^{20} cm^{-3} to 1.2×10^{20} cm^{-3}. As for Zr and N18, the N_D changed a little after hydrogen permeation. Additionally, it could be found that the N_D of the oxides has an inverse correlation to the estimated thickness by Eq. (1), which is consistent with the point defect model proposed by Macdonald [32,33]. The N_D behavior is in good agreement with the 'compacity' variation as shown in the EIS plots, demonstrating that the semiconductor properties are predominantly determined by the defective inner layer. To give a rational explanation for the different N_D variation after hydrogen permeation, it is inferred that the tin or niobium additive in Zr-4, N18 and M5 probably arouses significant differences.

Mechanism investigation

Based on the difference of the alloy composition, it may be deduced that the addition of niobium can enhance the hydrogen resistance of the oxides, while tin should have some connection with the degradation of the oxides in the reductive atmosphere. To test the hypothesis and further investigate the possible mechanism, PL test concerning the nature of the defects and XPS analysis regarding the electronic states of O1s, Zr3d, Sn3d and Nb3d were continuously implemented for the oxides before and after hydrogen permeation.

The PL spectra for oxides before and after hydrogen permeation are presented in Fig. 8. As for samples before hydrogen permeation, the intense peak at ~510 nm could be attributed to the involvement of oxygen vacancies in ZrO_2 and the short wavelength excitation (~420 nm) could be ascribed to the near band–edge transitions, similar to the results as reported by Liang et al. [34]. After hydrogen permeation, it is obvious that the peak at ~420 nm remain almost the same while the relative intensity of the peak at ~510 nm increased, suggesting that the concentration of oxygen vacancies increased after hydrogen permeation. It could also be seen that the shape of PL spectra for the oxides formed on different zircaloys were similar, implying that similar oxide phase and structures were obtained for different zircaloys before and

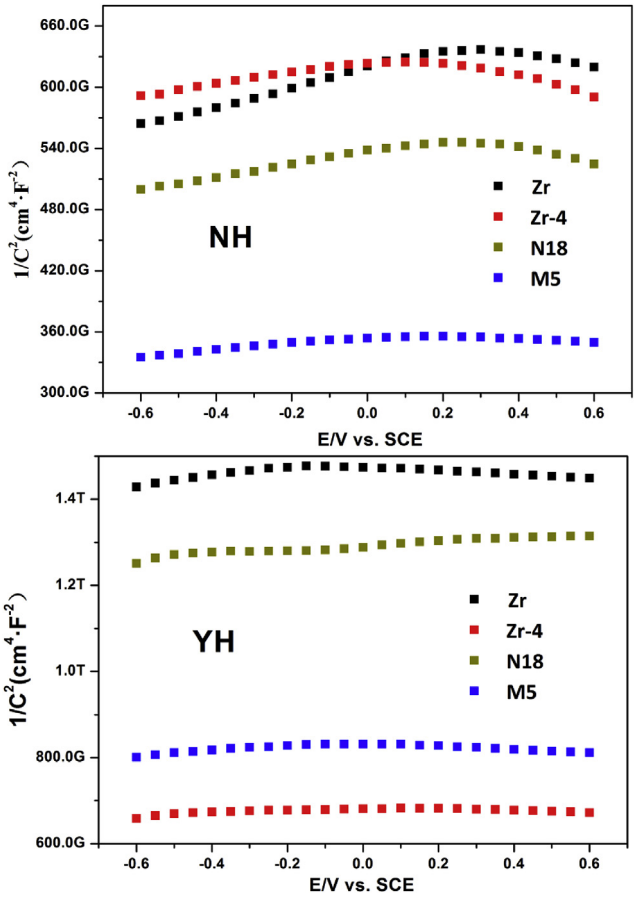

Fig. 6 – Mott–Schottky plots for the oxides formed on different zircaloys before and after hydrogen permeation.

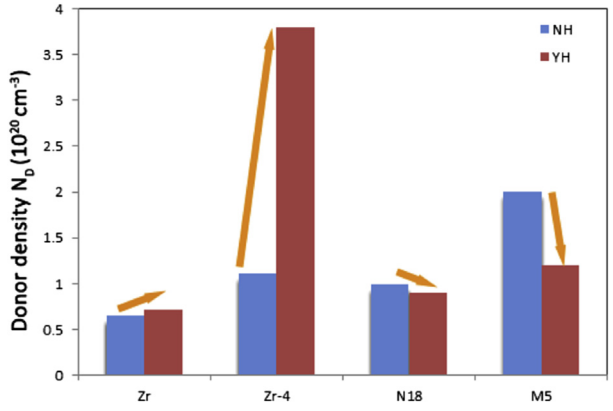

Fig. 7 – Donor density of the passive films formed on different zircaloys before and after hydrogen permeation.

after hydrogen permeation, which is in good agreement with the Raman spectra and EIS results (see in Figs. 3 and 5). However, the variation of peak position at ~510 nm between the oxides before and after hydrogen permeation is different. It did not change for zirconium after hydrogen permeation, while for other zircaloys, there is a red shift of the peak, probably due to the introduction of additional energy levels in the band gap of ZrO_2 caused by the Sn or Nb additives.

X-ray photoelectron spectroscopy is used to semi-quantitatively analyze the chemical state of the Zr, Sn and Nb elements. It is well documented that the binding energy (BE) of 2.4 eV represents the spin–orbit splitting between the Zr $3d_{5/2}$ and $3d_{3/2}$ peaks, while 8.4 eV represents splitting between the Sn $3d_{5/2}$ and $3d_{3/2}$ peaks and a 2.8 eV represents the splitting between the Nb $3d_{5/2}$ and $3d_{3/2}$ peaks [35–37]. The binding energy values of Zr3d peaks determined by Morant et al. (shown in Table 4) were considered as a reference in the present study, though the BE values in the literature were measured for the zirconium oxides formed in air or vapor water [38].

The curve deconvolution of the XPS spectra of Zr3d peaks was performed and the corresponding percentage of identified components was calculated. Fig. 9 shows the multi-peak fitted Zr3d spectra measured for the oxide layers on different zircaloys before and after hydrogen permeation. The fitting results of BEs for $Zr3d_{5/2}$ are summarized in Table 5. As shown, before hydrogen permeation the zirconium oxides were mainly composed of two or three different chemical states except for the oxide formed on Zr-4, which shows one single oxide state $Zr3d_{5/2}$ BEs at 181.97 eV. Comparing the results listed in Table 4, one can find that the as-prepared zirconium oxides were predominantly sub-stoichiometric. To give a comprehensive comparison, a calculation method was proposed to estimate the average binding energy values of $Zr3d_{5/2}$ (denoted as $\overline{BE}$) in the oxides formed on the different zircaloys, as the following.

$$\overline{BE} = \sum_{1}^{i} (BE_i \times w_i\%) \quad (5)$$

Where, BE_i is the binding energy values of each identified oxide and $w_i\%$ is the corresponding percentage. The calculated $\overline{BE}$ s are 182.42, 181.97, 182.15, 182.29 eV for Zr-NH, Zr4-NH, N18-NH and M5-NH, respectively. As for the oxides after hydrogen permeation, the $\overline{BE}$ s are 182.16, 182.33, 182.17, 182.44 eV for Zr-YH, Zr4-YH, N18-YH and M5-YH, respectively. It is clear that the as-prepared multiple oxides seem to react and finally transformed to a single oxide. As shown in Table 5, the $\overline{BE}$s of Zr3d shows a shift of 0.36, 0.02 and 0.15 eV to higher binding energy after hydrogen permeation for Zr-4, N18 and M5, respectively, while for zirconium $\overline{BE}$s shifts to a lower value, an inverse $\overline{BE}$s variation (−0.26 eV) compared to that of the other zircaloys, implying that the addition of alloying elements like tin or niobium can modulate the behavior of redox reaction of zirconium oxides in the reductive atmosphere.

Fig. 10 shows the multi-peak fitted Sn3d spectra for the oxides formed on Zr-4 and N18 before and after hydrogen permeation. The Sn3d scan for the oxides formed on Zr and M5 did not show the existence of tin element, which in consistent with the chemical composition results. The fitting results for $Sn3d_{5/2}$ were shown in Table 6. The BE at around 486.2 eV was assigned to SnO_{2-x}, and a BE at lower energy (485 eV) for N18-NH was attributed to the metallic Sn phase. Obviously, unlike the BE variation of $Zr3d_{5/2}$, $\overline{BE}$ of $Sn3d_{5/2}$ for Zr-4 shows a shift of −0.41 eV after hydrogen permeation, while $\overline{BE}$ for N18 shows a small increase, from 485.86 eV to 485.94 eV. As to the Nb3d profile for the oxides formed on M5, a BE of $Nb3d_{5/2}$ at 207.44 is identified, probably due to the

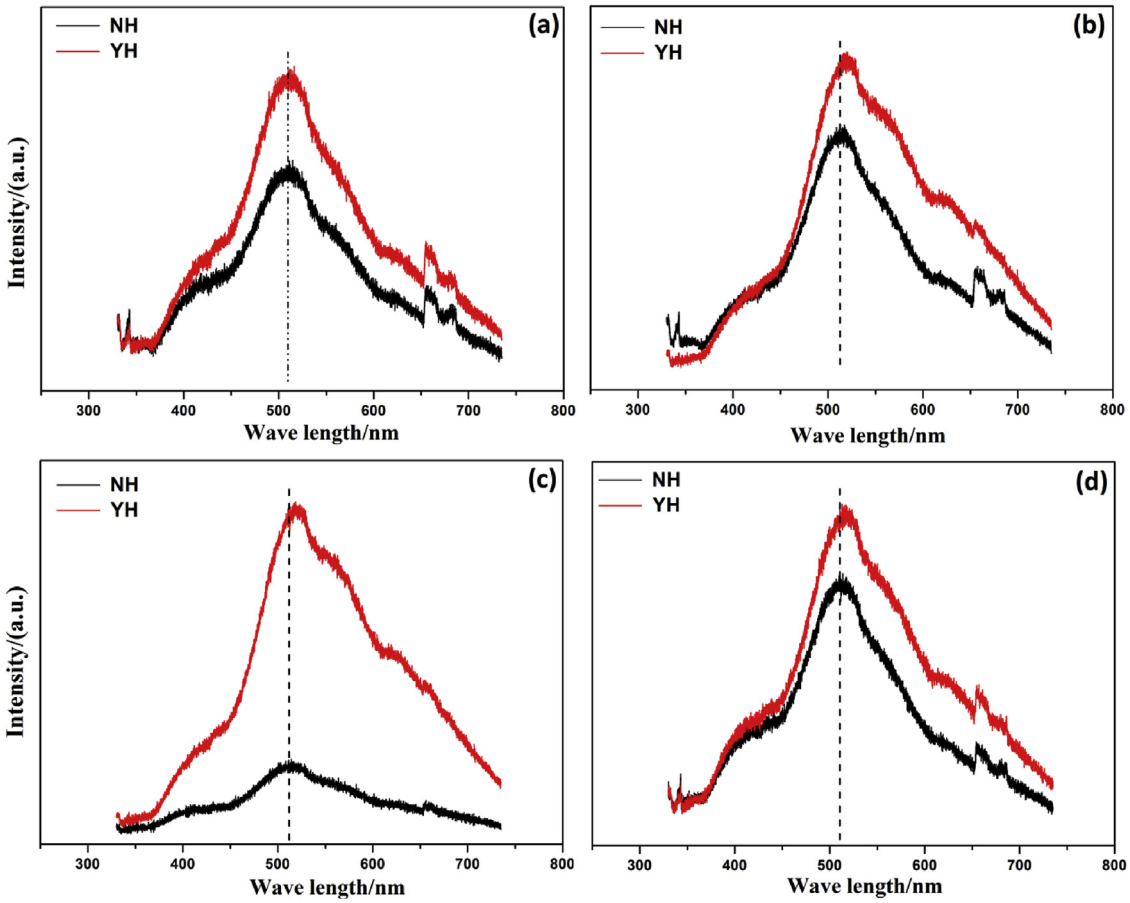

Fig. 8 – PL spectra for the oxides formed on different zircaloys before and after hydrogen permeation: (a) Zr, (b) Zr-4, (c) N18, and (d) M5.

Table 4 – Zr3d binding energies (eV) used in deconvolution of XPS spectra.

Component	Zr $3d_{5/2}$	Zr $3d_{3/2}$
Clean Zr	178.8	181.1
$Zr^{I}(Zr_2O)$	179.7	182.1
$Zr^{II}(ZrO)$	180.8	183.2
$Zr^{III}(Zr_2O_3)$	181.8	184.2
$Zr^{IV}(ZrO_2)$	182.9	185.3

formation of Nb_2O_5. After hydrogen permeation, the $Nb3d_{5/2}$ peak shifts from 207.44 to 206.62 eV. These suggested that reduction of niobium oxides should have taken place after hydrogen permeation. However, the peak intensity of Nb3d is much lower than that of Sn3d, indicating a less niobium content in the oxides. The observed phenomenon was consistent with earlier reports that all tin present in the metal passes into the oxide along with zirconium as hydrothermal corrosion progresses while niobium is rejected from the oxide during corrosion [39].

In our study, the composite oxides before hydrogen permeation were modulated to an equilibrium state after hydrogen permeation. From the XPS profiles of Zr3d, Sn3d and Nb3d, it seems that the oxygen ions in the near-stoichiometric niobium oxides and tin oxides were extracted by the sub-stoichiometric structure of ZrO_{2-x}, causing the transformation to near-stoichiometric zirconium oxides. Nevertheless, it should be noted that the XPS measurement only reveals the chemical state on the surface within a few nanometers. Since hydrogen passes into the whole oxide as decided by the EIS plots, it is safe to presume that changes of the oxidation states in the inner dense layer is similar to that of the outer porous layer.

To find the possible state of hydrogen in the oxide, curve deconvolution for the XPS spectra of O1s peaks was shown in Fig. 11. As for the oxides before hydrogen permeation, peaks at BEs around 529 and 530 eV are attributed to the oxidic oxygen O^{2-}, and the lower intensity component at 532.6 eV was assigned to the hydroxyl species –OH, i.e. the physically absorbed water. The fitting results of O1s spectra are summarized in Table 7. It could be seen that except for a peak centered at ~530 eV belonging to the oxidic species, another peak was identified at ~530.7 eV after hydrogen permeation, which is unlikely to be the physical absorbed water species. From the fitting results of Zr3d as shown in Table 5, it is clear that after hydrogen permeation, the multiple states of Zr3d transformed to a single state. Therefore, it is conjectured that the emerging oxygen component at ~530.7 eV may result from the formation of hydrogen defects OH_O and the corresponding component percentages were 55%, 56.6%, 66.8% and 59.1% for Zr-YH, Zr-4-YH, N18-YH and M5-YH, respectively. The difference is probably due to the percentage and size of precipitates,

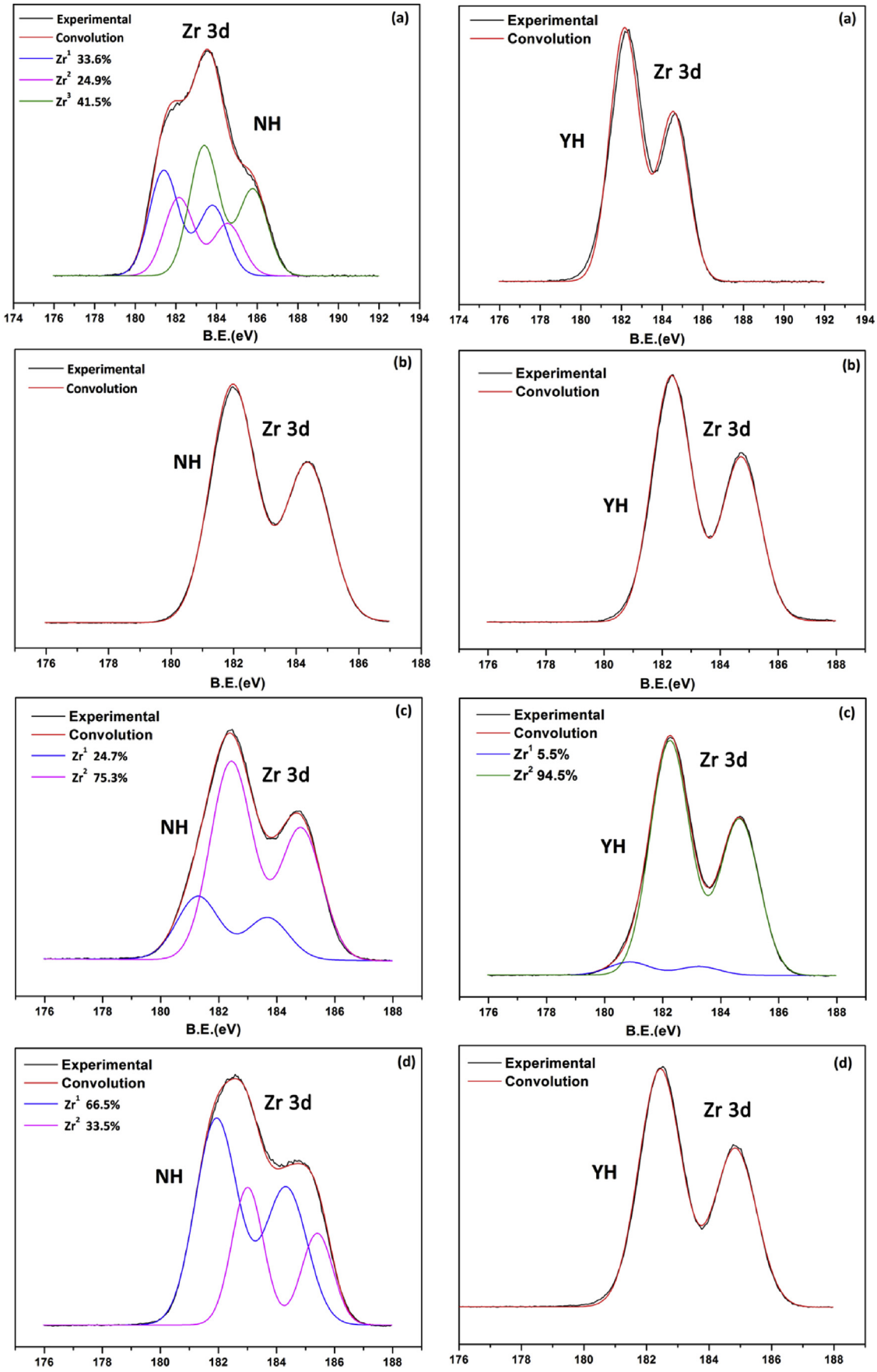

Fig. 9 – Multi-peak fitted Zr3d spectra for the oxides formed on different zircaloys before and after hydrogen permeation: (a) Zr, (b) Zr-4, (c) N18, and (d) M5.

Table 5 – Summary of the binding energy of the intensity peak(s) in the Zr3d.

Samples	Binding energy (eV)					
	Zr $3d_{5/2}$ NH				Zr $3d_{5/2}$ YH	
	Zr-1	Zr-2	Zr-3	$\overline{BE_{NH}}$	Zr-1	Zr-2
Zr	181.41	182.15	183.39	182.42	–	182.16
Zr-4	–	181.97	–	181.97	–	182.33
N18	181.28	182.43	–	182.15	180.86	182.25
M5	–	181.93	183.01	182.29	–	182.44

Table 6 – Summary of the binding energy of the intensity peak(s) in the Sn3d.

Samples	Binding energy (eV)			
	Sn $3d_{5/2}$ NH			Sn $3d_{5/2}$ YH
	Sn-1	Sn-2	$\overline{BE_{NH}}$	Sn-2
Zr-4	–	486.29	486.29	485.88
N18	484.99	486.14	485.86	485.94

as we know that the interface between second phase particles and oxides is a trapping center for the hydrogen [16].

To sum up, experimental phenomena and results can be summarized as follows.

(1) The oxide thickness given by AES, phase type and surface morphology remains almost intact, and the dominant defects in the oxides are oxygen vacancies.
(2) From the XPS profiles of O1s spectra and AES results, the absorbed hydroxyl species cannot be neglected and thus acted as oxygen sources.
(3) From the EIS, the inner dense layer should be more effective to protect from hydrogen permeation through the oxides compared to the outer porous one.
(4) It has been previously proposed that the transformation of sub-stoichiometric zirconium oxide to a near stoichiometric one is one of the main factors causing instability or degradation of the inner barrier layer [40].

A decrease of O/Zr ratio in the inner layer was observed from the AES for N18-YH and M5-YH, in accordance of the 'compacity' increase shown in the phase plots. Therefore, the less compact inner layer of Zr-YH and Zr-4-YH is probably due to the formation of near-stoichiometric zirconium oxides in the inner layer. Since the main difference of the as-received zircaloys lies in the chemical composition, it is rational to deduce that the different oxygen ion behavior aroused by tin and niobium additives respectively leads to the different 'compacity' change of the inner layer during hydrogen permeation.

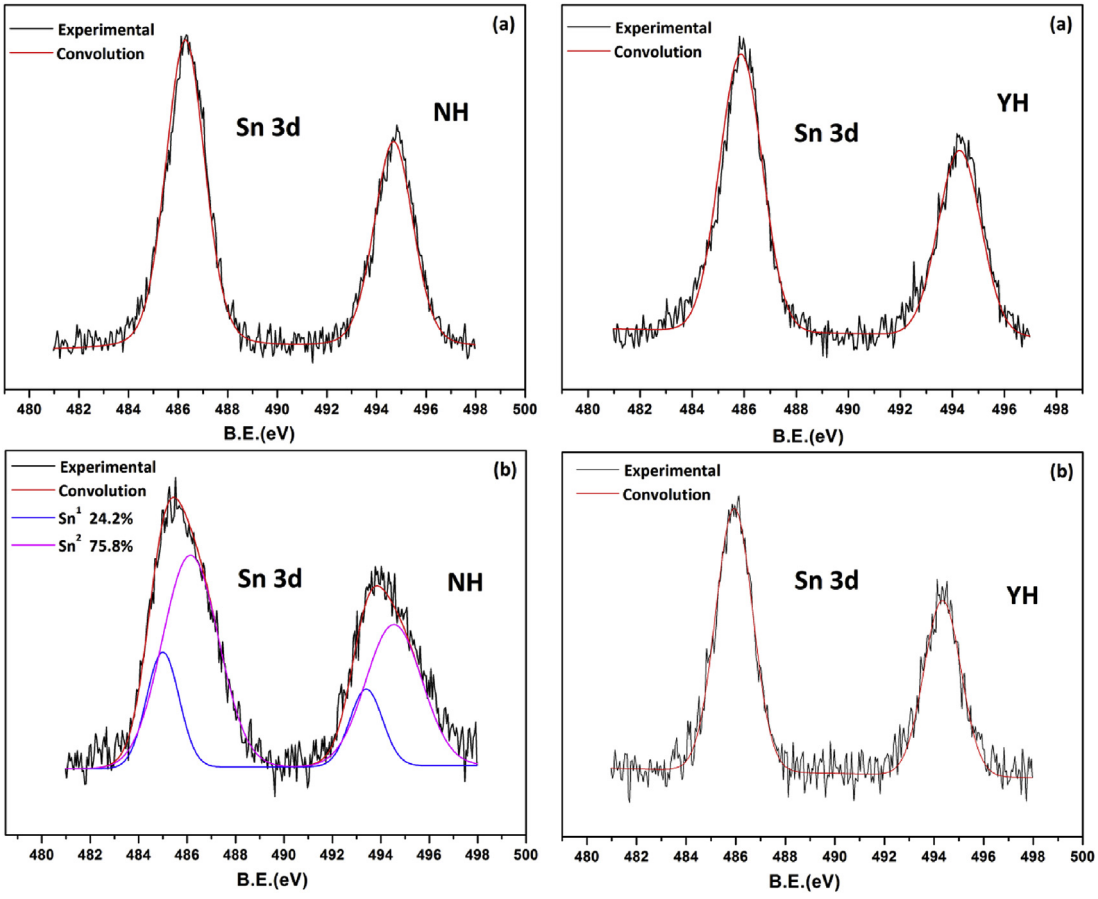

Fig. 10 – Multi-peak fitted Sn3d spectra for the oxides formed on different zircaloys before and after hydrogen permeation: (a) Zr-4 and (b) N18.

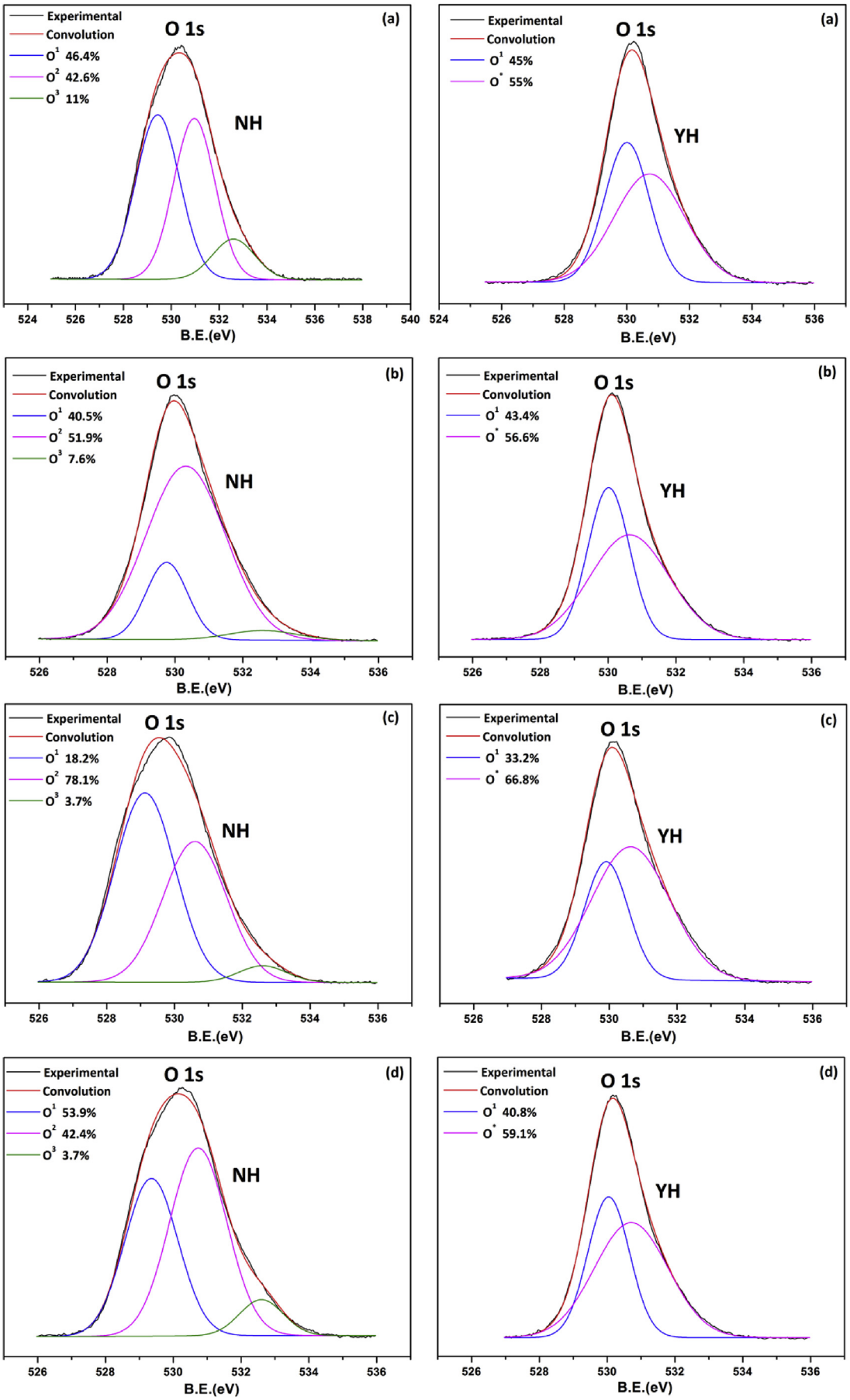

Fig. 11 – Multi-peak fitted O1s spectra for the oxides formed on different zircaloys before and after hydrogen permeation: (a) Zr, (b) Zr-4, (c) N18, and (d) M5.

Table 7 – Summary of the binding energy of the intensity peak(s) in the O1s.

Samples	Binding energy (eV)				
	O 1s NH			O 1s YH	
	O-1	O-2	O-3	O-1	$OH_O^{\cdot}$
Zr	529.4	531.0	532.6	530.0	530.7
Zr-4	529.8	530.3	532.6	530.0	530.6
N18	529.1	530.6	532.6	529.9	530.6
M5	529.4	530.7	532.6	530.0	530.7

Based on these observations and analyses, a possible mechanism is proposed to explain the alloying element effect of tin and niobium on the behavior of oxides in the hydrogen permeation condition. Schematic illustration of the possible mechanism was shown in Fig. 12. From Fig. 12, several reactions occurred in the reductive atmosphere, which could be divided into three different types. It should be pointed out that the valence states of zirconium, tin and niobium ions shown in Fig. 12 are probably not the exact states, i.e. here all the presented valence states were just taken as an example to illustrate the possible valence state variation for these different elements.

Type I includes the formation of oxygen vacancies and hydrogen defects. As shown in the PL (Fig. 8) and XPS (Fig. 11) results, it is reasonably assumed that the oxygen vacancies and hydrogen defects act as the intermediate products or the modulator for all relevant reactions.

Type II tried to explain the XPS profiles of Sn3d and Nb3d spectra, and the different N_D variation behavior for the passive films formed on different types of zircaloys. As shown, the reduction of tin ions causes the increase of oxygen vacancy concentration and thus increases the N_D. As for niobium ions, except for the reduction reaction, more zirconium ions were substituted with the niobium ions, causing an increase of the zirconium vacancy concentration. Therefore, the oxygen was ejected from the inner layers and thus causes the increase of Zr/O ratio as seen in the depth profiles (Fig. 4) of N18 and M5, which stabilizes the inner layer for the reason discussed above.

Type III is proceeded with Type II. On the reduction of zirconium, tin and niobium ions, the steam or its decomposition product fills the vacancies and thus results in the superficial inward diffusion of oxygen ions.

Type IV is related to the disproportionated reactions, as shown in Tables 5 and 6.

Type I:

$$\text{I}-1\quad \textit{Dissociation of } H_2O \text{ and } H_2 \begin{cases} H_2O \rightarrow OH' + H^{\cdot} \\ H_2 \rightarrow 2H \rightarrow 2H^{\cdot} + 2e' \end{cases}$$

$$\text{I}-2\quad \textit{Formation of } V_O^{\cdot\cdot} \text{ in } ZrO_2 : O_O + 2H \rightarrow V_O^{\cdot\cdot} + H_2O + 2e'(ZrO_2)$$

$$\text{I-3}\quad \textit{Formation of } OH_O^{\cdot} \begin{cases} V_O^{\cdot\cdot} + H_2O \rightarrow OH_O^{\cdot} + H^{\cdot} \\ V_O^{\cdot\cdot} + OH' \rightarrow OH_O^{\cdot} \\ O_O + H^{\cdot} \rightarrow OH_O^{\cdot} \end{cases}$$

Type II:

$$\text{II-1}\quad \textit{Defect reaction of } Sn^{4+}: SnO \xrightarrow{SnO_2} Sn_{Sn}'' + O_O + V_O^{\cdot\cdot}$$

$$\text{II-2}\quad \textit{Defect reaction of } Nb^{5+} \begin{cases} Nb_2O_3 \xrightarrow{Nb_2O_5} 2Nb_{Nb}'' + 3O_O + V_O^{\cdot\cdot} \\ 2Nb_2O_5 \xrightarrow{ZrO_2} 4Nb_{Zr}^{\cdot} + V_{Zr}'''' + 10O_O^X \end{cases}$$

Type III:

$$\textit{Inward diffusion of O} \begin{cases} V_O^{\cdot\cdot} + H_2O(g) \rightarrow O_O + 2H^{\cdot} \\ V_O^{\cdot\cdot} + OH' \rightarrow OH_O^{\cdot} \end{cases}$$

Type IV:

$$\text{Disproportionated reaction} \begin{cases} 2Zr^{3+} + Sn^{4+} \rightarrow 2Zr^{4+} + Sn^{2+} \\ 2Zr^{3+} + Nb^{5+} \rightarrow 2Zr^{4+} + Nb^{3+} \end{cases} (BE_{Zr3d}\uparrow, BE_{Sn3d}\downarrow, BE_{Nb3d}\downarrow)$$

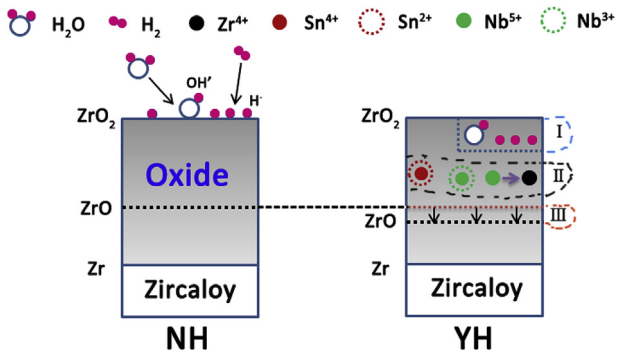

Fig. 12 – Schematic illustration of the possible mechanism.

Conclusions

Oxide films with hundreds of nanometers in thickness were fabricated hydrothermally on four different types of zircaloys for 24 h at 200 °C in pure water. The hydrogen permeation characteristic was characterized by a series of techniques. The principal findings and conclusions of this work are as follows:

(1) The predominant phase of the oxides before and after hydrogen permeation is monoclinic ZrO_2. Electrochemistry analysis suggests that nature of the oxide structure maintains the same after hydrogen permeation. The oxide is globally constituted of two layers, the outer one being porous, the inner one being dense and defective.

(2) Mott–Schottky analysis shows that the inner layer is n-type in electronic character and the PL spectra indicate that the concentration of oxygen vacancies increases

after hydrogen permeation. The protective character (defined as 'compacity') shows various behaviors for different zircaloys. As for Zr and Zr-4, the compacity of the inner layer decreases after hydrogen permeation, but for N18 and M5, the protective character increases. The alloying element effect of tin or niobium may be related to the different permeation behavior of the oxides.

(3) In a reductive environment, the sub-stoichiometric zirconium oxide is inclined to capture the oxygen from near-stoichiometric tin oxides or niobium oxides. The reduction of tin ions causes the 'compacity' loss of the inner layer, while the reduction of niobium ions combining its doping effect reduces the donor density of the passive films and thus enhances the hydrogen resistance.

Strictly speaking, the above mechanism proposed is based partially on different surface analyses. For a reasonable and exact explanation, further work such as dynamic cross section element will be required in the future. Although much work still needs to be done in discovering the real hydrogen diffusion process, we believed that this work might provide some insights in understanding the mechanism.

Acknowledgment

This research was funded by the National Basic Research Program of China (973 Program) under grant No. 2011CB61050, the NSAF program (No. U1430118), the Chinese National Fusion Project for ITER (No. 2013GB110000), the State Key Laboratory of Surface and Chemistry, China Academy of Engineering Physics (No. SPC 201102), the Reactor Fuel and Materials Laboratory, Nuclear Power Institute of China (Grant No. STRFML-2013-05), and the 56th China Postdoctoral Science Foundation (Grant No. 2014M560980).

REFERENCES

[1] Shestakov V, Pisarev A, Sobolev V, Kulsartov S, Tazhibaeva I. Gas-driven deuterium permeation through F82H martensitic steel. J Nucl Mater 2002;307:1494–7.
[2] Panasyuk VV, Andreykiv OY, Gembara OV. Hydrogen degradation of materials under long-term operation of technological equipment. Int J Hydrogen Energy 2000;25:67–74.
[3] Kim JH, Choi BK, Baek JH, Jeong YH. Effects of oxide and hydrogen on the behavior of Zircaloy-4 cladding during the loss of the coolant accident (LOCA). Nucl Eng Des 2006;236:2386–93.
[4] Suman S, Khan MK, Pathak M, Singh RN, Chakravartty JK. Hydrogen in zircaloy: mechanism and its impacts. Int J Hydrogen Energy 2015;40:5976–94.
[5] Oudriss A, Creus J, Bouhattate J, Conforto E, Berziou C, Savall C, et al. Grain size and grain-boundary effects on diffusion and trapping of hydrogen in pure nickel. Acta Mater 2012;60:6814–28.
[6] Long JH, Gong H. Phase stability and mechanical properties of niobium dihydride. Int J Hydrogen Energy 2014;39:18989–96.
[7] Conic D, Gradisek A, Radakovic J, Iordoc M, Mirkovic M, Cebela M, et al. Influence of Ta and Nb on the hydrogen absorption kinetics in Zr-based alloys. Int J Hydrogen Energy 2015;40:5677–82.
[8] Ivanova SV. Effect of hydrogen on serviceability of zirconium items in VVER and RBMK-type reactors fuel assemblies. Int J Hydrogen Energy 2002;27:819–24.
[9] Zhang GK, Chen CA, Luo DL, Wang XL. An advance process of aluminum rich coating as tritium permeation barrier on 321 steel workpiece. Fusion Eng Des 2012;87:1370–5.
[10] Nakamichi M, Nakamura H, Hayashi K, Takagi I. Impact of ceramic coating deposition on the tritium permeation in the Japanese ITER-TBM. J Nucl Mater 2009;386–88:692–5.
[11] Bagwell RB, Messing GL, Howell PR. The formation of alpha-Al_2O_3 from theta-Al_2O_3: the relevance of a "critical size" and: diffusional nucleation or "synchro-shear"? J Mater Sci 2001;36:1833–41.
[12] Mudali UK, Dayal RK, Gnanamoorthy JB, Rodriguez P. Influence of thermal aging on the intergranular corrosion resistance of types 304LN and 316LN stainless steels. Metall Mater Trans A 1996;27:2881–7.
[13] Chen WD, Wang LJ, Lu SG. Influence of oxide layer on hydrogen desorption from zirconium hydride. J Alloy Compd 2009;469:142–5.
[14] Hermann A. Thermal behaviour of hydrogen in Zircaloy corrosion layers. J Nucl Mater 2002;302:217–9.
[15] Legrand E, Bouhattate J, Feaugas X, Garmestani H. Computational analysis of geometrical factors affecting experimental data extracted from hydrogen permeation tests: II – consequences of trapping and an oxide layer. Int J Hydrogen Energy 2012;37:13574–82.
[16] Lim BH, Hong HS, Lee KS. Measurements of hydrogen permeation and absorption in zirconium oxide scales. J Nucl Mater 2003;312:134–40.
[17] Gu J-J, Ling Y-H, Zhang R-Q, Dai X, Bai X-D. Properties of passive nano films on zircaloy-4 affected by defects induced by hydrogen permeation. Chin Phys B 2014;23.
[18] Rui T, Xiaoxue Y. Study on terminal solid solubility of hydrogen in N18, Zry-4 and M5 zirconium alloys. Chin J Mater Res 2009;23:635–9.
[19] Rotole JA, Sherwood PMA. Diaspore (beta-AlOOH) by XPS. Surf Sci Spectra 1998;5:46–52.
[20] McIntyre NS, Davidson RD, Weisener CG, Good GM, Mount GR, Warr BD, et al. Migration of hydrogen through thin-films of ZrO_2 on Zr-Nb alloy. J Vac Sci Technol A 1991;9:1402–5.
[21] Cox B. Pore structure in oxide-films on irradiated and unirradiated zirconium alloys. J Nucl Mater 1987;148:332–43.
[22] Bouvier P, Godlewski J, Lucazeau GA. Raman study of the nanocrystallite size effect on the pressure-temperature phase diagram of zirconia grown by zirconium-based alloys oxidation. J Nucl Mater 2002;300:118–26.
[23] Can L, Meijun L. UV Raman spectroscopic study on the phase transformation of ZrO_2, Y_2O_3-ZrO_2 and SO_4^{2-}/ZrO_2. J Raman Spectrosc 2002;33:301–8.
[24] Liu W, Zhu X, Wang X, Li Q, Yao M, Zhou B. Effect of Nb and Fe on corrosion resistance of zirconium alloys. Atomic Energy Sci Technol 2010;44:1477–81.
[25] Chen YZ, Urquidi-Macdonald M, Macdonald DD. The electrochemistry of zirconium in aqueous solutions at elevated temperatures and pressures. J Nucl Mater 2006;348:133–47.
[26] Cox B, Gascoin F, Wong YM. Properties of thin anodic oxide-films on zirconium alloys. J Nucl Mater 1995;218:113–28.
[27] Goossens A, Vazquez M, Macdonald DD. The nature of electronic states in anodic zirconium oxide films part .1. The potential distribution. Electrochim Acta 1996;41:35–45.

[28] Barberis P, Frichet A. Characterization of Zircaloy-4 oxide layers by impedance spectroscopy. J Nucl Mater 1999;273:182–91.
[29] Barker JR, Ferry DK. On the physics and modeling of small semiconductor-devices .1. Solid-State Electron 1980;23:519–30.
[30] Dutoit EC, Vanmeirhaeghe RL, Cardon F, Gomes WP. Investigation on frequency-dependence of impedance of nearly ideally polarizable semiconductor electrodes CdSe, CdS and TiO_2. Ber Bunsen Phys Chem 1975;79:1206–13.
[31] Meisterjahn P, Hoppe HW, Schultze JW. Electrochemical and XPS measurements on thin oxide-films on zirconium. J Electroanal Chem 1987;217:159–85.
[32] Macdonald DD, Urquidimacdonald M. Theory of steady-state passive films. J Electrochem Soc 1990;137:2395–402.
[33] Macdonald DD. The point-defect model for the passive state. J Electrochem Soc 1992;139:3434–49.
[34] Liang JH, Deng ZX, Jiang X, Li FL, Li YD. Photoluminescence of tetragonal ZrO_2 nanoparticles synthesized by microwave irradiation. Inorg Chem 2002;41:3602–4.
[35] Nishino Y, Krauss AR, Lin YP, Gruen DM. Initial oxidation of zirconium and Zircaloy-2 with oxygen and water vapor at room temperature. J Nucl Mater 1996;228:346–53.
[36] Vanattekum P, Trooster JM. Bulk-plasmon-loss and surface-plasmon-loss intensities in photoelectron, Auger, and electron-energy-loss spectra of Mg metal. Phys Rev B 1979;20:2335–40.
[37] Latta EE, Ronay M. Catalytic oxidation of niobium. Phys Rev Lett 1984;53:948–51.
[38] Morant C, Sanz JM, Galan L, Soriano L, Rueda F. An XPS study of the interaction of oxygen with zirconium. Surf Sci 1989;218:331–45.
[39] Wei J, Frankel P, Polatidis E, Blat M, Ambard A, Comstock RJ, et al. The effect of Sn on autoclave corrosion performance and corrosion mechanisms in Zr-Sn-Nb alloys. Acta Mater 2013;61:4200–14.
[40] Park DJ, Park JY, Jeong YH. Microstructural analysis and XPS investigation of nodular oxides formed on Zircaloy-4. J Nucl Mater 2011;412:233–8.